ACS MATERIALS LETTERS

www.acsmaterialsletters.org

LETTER

One-Pot Confined Epitaxial Growth of 2D Heterostructure Arrays

Dechao Geng,* Ibrahim Abdelwahab, Xiaofei Xiao, Adrian Cernescu, Wei Fu, Vincenzo Giannini, Stefan A. Maier, Lin Li,* Wenping Hu, Kian Ping Loh, and Hui Ying Yang*

Cite This: *ACS Materials Lett.* 2021, 3, 217–223

Read Online

ACCESS | Metrics & More | Article Recommendations | Supporting Information

ABSTRACT: **Graphene and hexagonal boron nitride (*h*-BN) have attracted intensive interests in very recent years because of their unique physical and chemical properties. With similar crystal structures, graphene and *h*-BN pose great potential for constructing interesting heterostructures. Here, one-pot confined synthesis of large-area graphene/*h*-BN in-plane heterostructure arrays via sequential edge-epitaxy is first realized on liquid Cu surface. Extensive characterizations confirm the in-plane continuity between graphene and *h*-BN for the synthesized heterostructures. With increased growth time, the heterostructure arrays can be turned into a uniform centimeter-scale graphene/*h*-BN monolayer film. Furthermore, the plasmonic characteristics of the heterostructures are investigated and utilized to evaluate the quality of the hybrid structures. Our work demonstrates the designability of CVD process for large-area synthesis of graphene/*h*-BN heterostructures arrays, which might be generally applied to other 2D materials.**

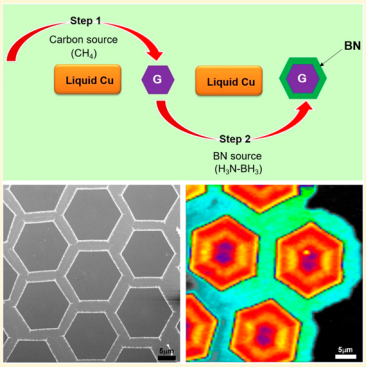

Graphene and hexagonal boron nitride (*h*-BN) are two representative 2D atomic crystals possessing similar honeycomb crystal structures with a lattice constant difference of only 2%. While graphene is a zero-bandgap semiconductor with remarkably high carrier mobility at room temperature,[1−3] atomically thin layer of *h*-BN is a dielectric with a wide bandgap of ∼5.9 eV.[4−6] Accordingly, if 2D domains of graphene and *h*-BN could be precisely engineered, hybrid structures with interesting properties and applications would be realized. Graphene/*h*-BN hybrid structures can exist in various configurations. It has been widely reported that graphene could be directly grown onto h-BN, resulting in formation of vertical heterostructure.[7] Within the configuration, the size and quality can be modulated with the aid of underneath *h*-BN. Furthermore, the other hybrid kind is a laterally stitched graphene and *h*-BN heterostructure. Owing to the extremely similar atomic lattice between graphene and *h*-BN, epitaxial growth will take place along the interfacial area. With the controllability over spatial configuration, graphene and *h*-BN heterostructures show great potential in optics, electronics and spintronics.[8] Formed by merging graphene and *h*-BN into a single atomic layer, the in-plane heterostructure has drawn intensive interests.[9−13] Exciting physical properties were predicted for such in-plane heterostructures.[14−17]

Owing to its high controllability, low loss, and large scalability, chemical vapor deposition (CVD) has been widely employed as a particularly effective method in fabricating 2D materials.[18] As for the case of graphene and *h*-BN heterostructures, sequential or continuous growth on catalytic metal surfaces via CVD has been reported.[12,19,20] Templated growth of *h*-BN starting from CVD graphene edges on copper foil was realized with lattice coherency of the two crystals.[10] However, to date, growth of graphene/BN heterostructures via CVD process is generally conducted at low pressure, resulting in irregular shapes and random edge directions. Furthermore, the size of the heterostructures is limited to micrometer scale, thus largely hindering further applications. Another challenge is related to the orientation of the heterostructure—that is, the as-grown samples are randomly dispersed and the production of highly orientated heterostructures has not yet been realized. Considered those concerns, if graphene and *h*-BN can be seamlessly stitched together with aligned orientation in a large scale, hybrid atomic layers with novel properties and further interesting applications could be created.

Here, we demonstrate for the first time one-pot confined synthesis of large-area hexagonal graphene/*h*-BN (h-G-*h*-BN) in-plane heterostructure arrays. The extremely uniform surface of liquid Cu enables the high throughput alignment of the first growing graphene domains and the subsequently grown *h*-BN peripheries, resulting in formation of lateral heterostructure

Received: November 3, 2020
Accepted: January 6, 2021

https://dx.doi.org/10.1021/acsmaterialslett.0c00517
ACS Materials Lett. 2021, 3, 217–223

arrays. Extensive characterizations confirm the in-plane continuity between graphene and *h*-BN. With increased growth time, centimeter-scale and uniform h-G-*h*-BN monolayer film is produced. Our work demonstrates the designability of CVD process for synthesis of 2D heterostructure arrays, offering a potential pathway for fabricating high-performance 2D-based electronic devices.

In our experiment, liquid Cu was used as the catalytic substrate, and methane (CH_4) and ammonia borane (H_3BNH_3, AB) were chosen as the precursors for graphene and *h*-BN growth, respectively.[21,22] To realize direct growth of G-BN structures, two strategies have been implemented (Figure S1). First, a small tube with one end sealed is used as holder of the AB powder. As that, the AB powder can be first sublimated into a stable flow rate gas into the small tube, rather than being randomly sublimated in the quartz tube. Second, another small tube with two open ends is introduced to hold the Cu catalyst, aiming for uniform deposition of active BN cluster or radicals.

The whole one-pot growth process is schematically illustrated in Figure 1a. A sequential growth strategy was

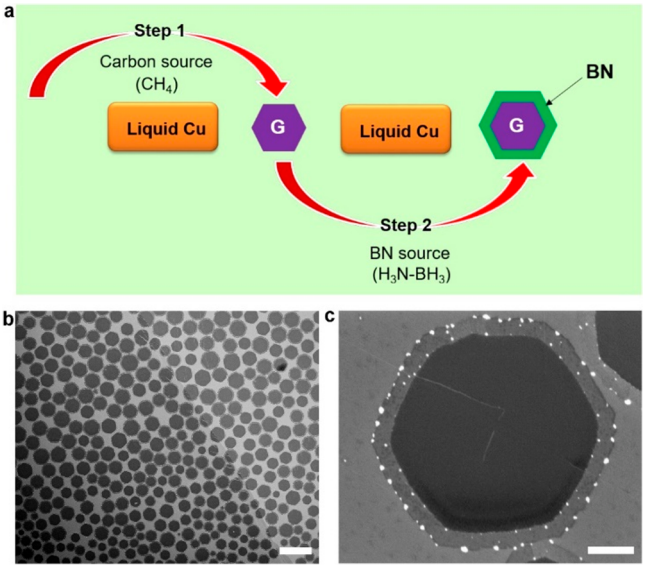

Figure 1. Continuous growth of G-BN in-plane heterostructure. (a) Schematic representation of the whole growth process. (b and c) SEM images of the large-area and single G-BN flakes, respectively, showing uniform distribution in size and morphology. The scale bar in panel b is 10 μm and in panel c is 1 μm.

employed, where graphene hexagon was first produced (Figure S2), and then, *h*-BN was epitaxially template grown along the graphene edges. The large-area h-G-*h*-BN in-plane heterostructure is clearly shown in Figures 1b and S3, where uniform distribution and size of the heterostructures are observed. It is worth noting that silicon oxides could be deposited onto the surface in the presence of white spots at high temperature (Figure S4). It is statistically conferred that the size of the heterostructures is mainly about 4 μm, while the size of intergraphene hexagons is around 3.3 μm (Figure S5), suggesting a uniform and homogeneous growth for both graphene and *h*-BN. As for the single h-G-*h*-BN heterostructure, at higher magnification, obvious contrast is observed between the graphene and *h*-BN due to the quite different electrical properties (Figure 1c). During the graphene growth period, regular hexagonal structures nucleated and grew, and their shape was preserved during the AB source heating period.

The heterostructures were transferred onto Si/SiO_2 substrate for further measurements, where thick graphene was occasionally observed onto the surface owing to excessive nucleation in the step of graphene growth (Figures S6 and S7). Figure 2a and b show the typical AFM images, where the

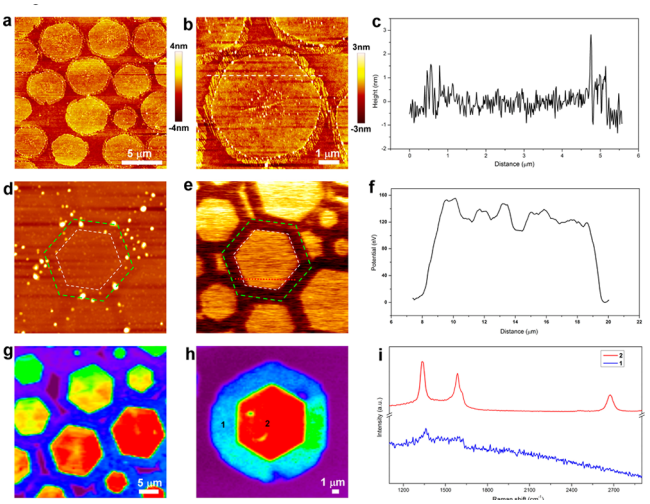

Figure 2. Characterization of the transferred G-BN in-plane heterostructure. (a) AFM image of large-area G-BN heterostructures, indicating an intact transfer process. (b) AFM image of single G-BN flake, where the outer BN ribbon displays wrinkle features, while the inner graphene is relatively flat. (c) Thickness profile of the single flake in (b), confirming the uniform surface of the graphene and *h*-BN monolayers. (d) Morphology image of a G-BN heterostructure, in which the contrast between the two materials is not obvious. (e) The corresponding electrostatic force microscopy (EFM) map of the heterostructure in (d), showing a clear contrast in the electrical potential between graphene and *h*-BN. (f) The potential profile of the heterostructure in panel e. (g and h) Raman mapping of the G-BN heterostructure, where the G and BN are differentiated by the color contrast. (i) The corresponding Raman spectra of the marked areas 1 and 2 in panel h, confirming the presence of G and BN.

profile of hexagonal graphene and *h*-BN ribbons are both clearly observed. As shown in Figure 2c, it is evidenced that uniformness in thickness across the whole surface is manifested, with a thickness around of 0.5 nm, confirming the monolayer features for both graphene and *h*-BN. To further characterize the interface between graphene and *h*-BN, electrostatic force microscope (EFM) is employed. Figure 2d shows the morphology image of the in-plane heterostructure, where the inner hexagonal graphene crystals and outer *h*-BN ribbons can be clearly differentiated. The potential EFM map (Figure 2e) reveals a large difference in the electrical potential contrast between graphene and *h*-BN. The obvious contrast difference is attributed to the different electrical properties of the conductive graphene and the insulating *h*-BN (Figure 2f).

Raman spectroscopy was further utilized to evaluate the presence of both graphene and *h*-BN in the hybrid structures. Figure 2g shows Raman map of the characteristic E_{2g} peak of the large-area graphene and BN heterostructures. Magnified mapping image (Figure 2h) further displays the detailed structural information. We have located two areas on inner graphene and outer BN and, then, collected their Raman

https://dx.doi.org/10.1021/acsmaterialslett.0c00517
ACS Materials Lett. 2021, 3, 217−223

signals, as shown in Figure 2i. For the inner graphene hexagons (marked area 2), the characteristic Raman peaks, 2D band (2690 cm^{-1}), G band (1580 cm^{-1}), and D band (1360 cm^{-1}) are all found. For the outer *h*-BN ribbon (marked area 2), a characteristic E_{2g} peak at 1370 cm^{-1} emerges, indicating that the h-BN ribbons are well crystallized. The EFM and Raman imaging results strongly confirm the continuity of the heterostructure between graphene and *h*-BN in the two-step CVD growth.

Given the structural similarity between graphene and *h*-BN, together with the observed continuous growth of *h*-BN along the edges of graphene, the concept of "confined growth" is proposed. While we have previously reported a controlled growth of large-area graphene arrays on liquid Cu surface,[21] the interplay between the first grown graphene hexagons and the following BN ribbons is strongly verified in this work. On the basis of this thought, we further realize a controlled graphene-confined growth of large-area h-G-*h*-BN arrays. First, self-aligned graphene arrays were produced (Table S1), and then *h*-BN growth was initiated and gradually expanded at the spaces among those graphene grains. Templated by the edges of graphene, the *h*-BN growth will be stopped once the neighboring ones emerged. In this case, the *h*-BN growth is completely confined by the graphene, where the size, morphology, and orientation of BN can be precisely engineered by just tuning the growth of graphene. It can be concluded that with further increased growth time, a monolayer film composed of orientated graphene and *h*-BN can be fully covered on the surface. The whole growth process is schematically illustrated in Figure 3a. The complete monolayer full film with centimeter-scale is readily fabricated with a growth time of 10 min, and the large-area SEM image is clearly shown in Figures 3b and S8. In this film, the hexagonal graphene array over a large area is observed, among which the *h*-BN filled up the rest areas. At higher magnification, the high orientation of *h*-G-*h*-BN array is much more obvious (Figure 3c), in which the interfacial parts between two neighboring *h*-BN ribbons are clearly detected. It is also worth noting that there exist clear white depositions along the edges of graphene hexagons. It is speculated that these depositions are thick BN crystals, originated from excessive introduction of BN source in the second growth stage. Due to the higher reactivity, the BN clusters or radicals would preferably deposit onto those edged areas (interfacial boundaries).

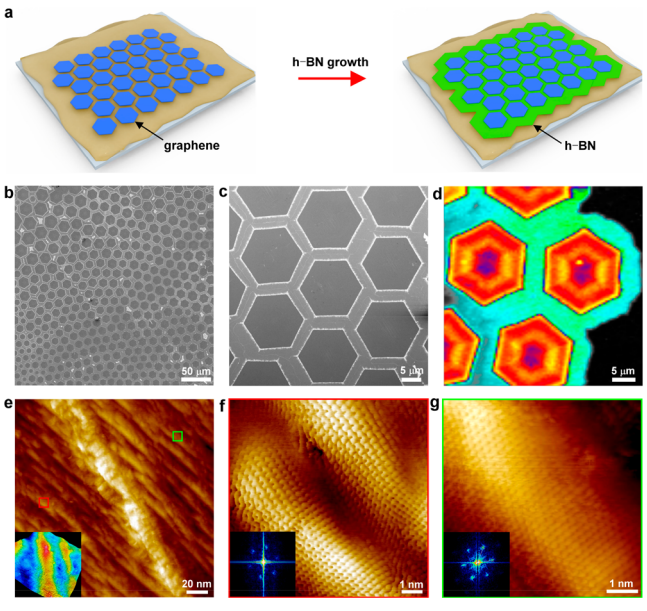

Figure 3. Characterization of highly arrayed G-BN heterostructures. (a) Schematic representation of growth of G-BN array initiated by graphene array. It can be seen that the BN growth is completely confined in the space areas among the graphene grains. (b and c) SEM images of the as-grown large-area G-BN monolayer film on liquid Cu surface, where the graphene arrays are clearly observed. It is noticeable that thick BN crystals are preferably deposited on the interfacial area between G and BN. (d) Raman mapping image of the orientated G-BN arrays. (e–g) STM images of the interfaced area between graphene and *h*-BN, where the measured corresponding areas are color labelled, respectively.

To characterize the confined *h*-G-*h*-BN monolayer film, AFM and Raman measurements have been conducted. The AFM images of a single graphene hexagonal flake are shown in Figure S9, along which the deposited BN crystals are observed at the edged areas, consistent with the SEM results (Figure 3c). Thickness determination and Raman characterization suggested that those aggregated *h*-BN crystals generally have three or four layers, with a thickness around 1-2 nm (Figures S10 and S11). Furthermore, it is seen that all the few-layer BN crystals are triangular shaped and with a pyramid structural feature.[22,23] Raman maps of the transferred samples are clearly shown in Figures 3d and S7, where the inner hexagonal graphene domains and outer BN are distinctly differentiated over the whole surface. All the above results strongly verified that a large-area and full monolayer film composed of highly orientated graphene and BN arrays can be further produced.

STM measurement has also been conducted on the heterostructure for imaging the graphene and *h*-BN surfaces at the atomic level. Figure 3e shows the STM image of one located interfacial area within the heterostructure, where obvious contrast is directly observed along the stitched line. It is seen that graphene and *h*-BN are present at the sides of the boundary, and 3D image (Figure 3e insets) further suggested the patching boundary. As discussed in the previous part, owing to the higher reactivity of the interfacial area, there might be more *h*-BN depositions, resulting in a larger boundary thickness when compared with those of individual graphene and *h*-BN monolayers. It is deduced that the graphene and *h*-BN in our case are seamless stitched at the scale of single-layer,[10] while excessive *h*-BN depositions onto the underlying patching boundaries are accounted for the thickness discrepancy (Figures S12 and S13). The two marked areas in Figure 3e at the sides of boundary have been further probed, where the results are mainly present in Figure 3f and 3g. It is found that the graphene and *h*-BN are corresponding to the red and green marked areas, respectively. Highly ordered atomic structures were observed for the graphene side, suggesting a high-crystalline feature, while hexagonal atomic structures were also found for the *h*-BN side, verifying a high-quality characteristic. The diffraction measurements (insets of Figure 3f and 3g) confirmed the presence of graphene and *h*-BN within the lateral heterostructure.

To investigate the plasmonic properties of the *h*-G-*h*-BN in-plane heterostructures, near-field signals have been collected using scattering-type scanning near-field optical microscopy (s-SNOM). Figure 4a illustrates the configuration of the s-SNOM imaging of localized graphene plasmon waves. When illuminated by an infrared laser beam, the tip acts as an optical antenna and can strongly convert the incident light into

https://dx.doi.org/10.1021/acsmaterialslett.0c00517
ACS Materials Lett. 2021, 3, 217–223

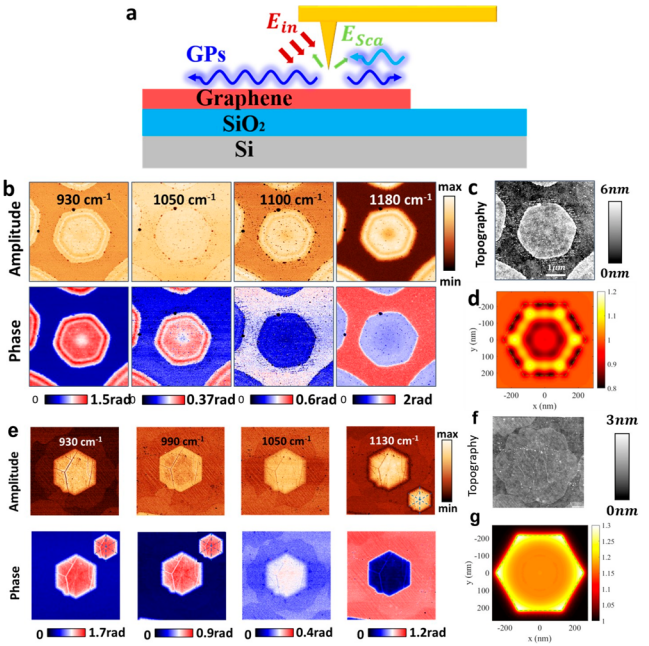

Figure 4. Near-field imaging of graphene structures and *h*-G-*h*-BN in-plan heterostructures. (a) Schematic of a typical s-SNOM experiment used to study graphene plasmons. (b) Real-space near-field images taken simultaneously with the AFM topography at four representative wavelengths. The evolution of the near-field contrast suggests that phase images are complementary to the amplitude images. (c) AFM topography of a single graphene flake. (d) Simulated near-field images of a hexagonal graphene structure at the wavelength of 930 cm^{-1} for different parameters. The dark dots around the edges are due to the excitation of edge modes. (e) Real-space near-field images of the *h*-G-*h*-BN structure at different wavelengths. The insets mark symmetric patterns with blue dashed lines. (f) AFM topography of a single *h*-G-*h*-BN flake. (g) Simulated near-field images of a hexagonal graphene structure at the wavelength of 930 cm^{-1} for different parameters.

a localized near field at the tip apex, providing the necessary momentum for launching plasmons on a graphene flake. The launched graphene plasmons propagate radially in all directions along the sheet and are reflected at boundaries. Interference patterns between the launched and edge-reflected plasmons are formed and collected by the tip. By varying the tip position, real-space near-field images can be obtained. Similarly, when other types of polaritons (for example, hyperbolic phonon polaritons in *h*-BN) are excited, these real-space images can also reflect the interference patterns of such polaritons (Figure S14). However, in our experiments, the used wavelengths are outside the Reststrahlen band of *h*-BN, and thus only graphene plasmons are considered here.

The optical amplitude and the corresponding phase of the near-field signals of such structure under several illumination wavelengths are illustrated in Figure 4b (Figures S15 and S16). The graphene sheet exhibits its intrinsic plasmonic property, which is attributed to its high crystalline quality. Figure 4c shows a typical AFM image of a graphene monolayer (without *h*-BN) array, where the profiles of the graphene structures are clearly observed. For all wavelengths considered, the rings due to the plasmon interference fringes are clearly visible in the optical amplitude and phase images around the edges of the imaged structures, which is consistent to the simulated result shown in Figure 4d. In Figure 4d, the carrier mobility and the Fermi energy (E_f) of graphene were set to 2000 $cm^2/(V{\cdot}s)$ and 0.4 eV, respectively. Another obvious feature is that the relative contrast between graphene and SiO_2 substrate strongly depends on the wavelength because of the strong Si−O phonon resonance and graphene plasmon−SiO_2 phonon coupling in this spectral range. As expected, Figure 4b clearly shows that plasmon wavelength and damping strongly depends on the illumination wavelength, being related to the optical constant of the SiO_2 substrate. Our experimental data also provide a convincing evidence that the phase images of the near-field signals could give a sharper contrast at certain wavelength range than the amplitude images, which is commonly used in previous studies, and thus, such phase images are complementary to the amplitude images.

Furthermore, interesting optical phase contrast and weaker amplitude contrasts are observed in the middle of the structures. In our s-SNOM experiments, these profiles are commonly observed for the graphene monolayer array. Considering that strain would be removed during the transfer process,[24] thus, we rule out strain variations across the flake as the source of the observed profiles. Most probably, they are related to the radial changes in carrier concentration (or the carrier mobility) caused by the formation of structural imperfection and chemical defects during the growth process. In the growth procedure of CVD-synthesized graphene structure, the center of the hexagon is initiated first, and thus is exposed to elevated temperatures for longest duration of time, introducing more defects. Similar phenomena have been reported in other single-crystalline CVD-synthesized materials, such as monolayer transition metal dichalcogenides.[25,26]

As it can be seen in Figure 4e, unintentional cracks and wrinkles are generated in the graphene sheets during transfer process. Figure S13 displays s-SNOM scanning of large-area *h*-G-*h*-BN heterostructures, revealing potentially large variation in doping concentration. Given the excellent capability of Raman spectroscopy for estimating the doping level in 2D materials, Raman mapping shown in Figure 2g is an evidence of such large variation of doping level across the sample, and Raman mapping in Figure 2h indicates the doping variation in a single graphene sheet. Such doped regions can change the local charge density, and thus modulate the bandgap of graphene. The nonuniform doping level across the sample is attributed to the relatively unstable supply of the BN source. Figure 4f shows a typical AFM image and a mechanical phase image of the transferred *h*-G-*h*-BN heterostructures, where the profile of hexagonal graphene and *h*-BN ribbons are clearly observed.

However, the nonuniform doping level within a single *h*-G-*h*-BN heterostructure is mainly due to the structural defects created during the growth process. For example, more B and N atoms may be substituted into graphene in the areas where more carbon vacancies (structural imperfections) exist, generating nonuniform doping level across the graphene flake. This is also supported by the Raman spectrum shown in Figure 2i. Although it is very common to find a D band signal in representative Raman spectra of graphene samples (such as the one shown in Figure 2i), such D band is not an intrinsic band of graphene monolayer and is originated from the surface contamination. For traditional CVD-grown graphene, the contamination is predominated by amorphous carbon introduced during the high-temperature synthetic process.[27] In our case, however, boron and nitrogen atoms may play the dominant roles in the formation of the D signal

https://dx.doi.org/10.1021/acsmaterialslett.0c00517
ACS Materials Lett. 2021, 3, 217−223

with such high intensity and broad width.[28] Furthermore, the appearance of the D* band (the shoulder of the G band), which is owing to the breaking of localized symmetry in graphene (i.e., the distortion of the lattice), is an evidence of the BN doping.[29,30] The BN doping is also reflected by the suppressed intensity of 2D band, possibly because of the strong photoluminescence background. Furthermore, we should bear in mind that the doping level may vary from region to region across the sheet, owing to complex factors (such as imperfections, stress, and temperature variation).

We also observed gradient profiles of optical amplitude existing around the edges of graphene flakes. This may be attributed to the possible variation of doping level[31] or compressive strain induced by the boundary of *h*-G-*h*-BN heterostructures, which can be suggested by the Raman mapping in Figures 2g and 3h. Another interesting feature is symmetric patterns (with a contrast gradient) existing in the near-field images of the *h*-G-*h*-BN heterostructures at certain wavelengths, as shown in the inset of the Figure 4f (Figurea S17 and S18). Interesting optical amplitude or phase contrasts concentrate at the hexagon center and radiated toward the six corners. Although a similar behavior has been reported in CVD-synthesized monolayer transition metal chalcogenides, such as WS_2, this is the first observation of such behavior in graphene flakes. We speculate that this feature is owing to the carrier concentration (or the carrier mobility) gradient originating from the formation of structural imperfection during crystal growth process and the resulting potential variation gradient in doping. The perfectly regular hexagonal shape of the graphene flakes with straight and sharp edges may also contribute to the formation of such symmetric patterns.

Our simulated results show that the graphene structure and the *h*-G-*h*-BN in-plan heterostructure should have almost the same s-SNOM signal images, when the same parameters of graphene and the surrounding materials are considered, and the illumination wavelength is outside the Reststrahlen band of BN (Figure 4g). However, the aforementioned high doping level, variation of carrier concentration across the sheet, structural imperfections and complex strain around the boundary of *h*-G-*h*-BN heterostructures introduced during the growth of *h*-G-*h*-BN heterostructures make the experimental s-SNOM imaging far away from the theoretical one. Owing to the scattering at the boundaries between dopants and graphene domains inside the doped graphene sheet, the carrier mobility is suspected to be much smaller than the mobilities reported for the pristine graphene. In addition, both the s-SNOM images and Raman mapping of the G-BN heterostructures suggest a high doping level in graphene. Previous experimental and theoretical studies have already indicated that Fermi energy up to 4.7 eV can be achieved in boron and nitrogen co-doped graphene sheets.[32] As such, in our corrected calculation shown in Figure 4g, the carrier mobility was considered as 100 $cm^2/(V{\cdot}s)$ and Fermi energy was set to $E_f = 3.0$ eV, which gave a better prediction. It should be noted that, when hyperbolic phonon polaritons in BN layer are excited, the graphene plasmon polaritons can be strongly coupled into the phonon polaritons of hexagonal BN in these in-plane G-BN heterostructures if the momenta of different polaritons match. Additionally, the transmittance between these two types of polaritons is controllable by tuning the graphene Fermi energy.[33] It also should be noticed that many factors, such as doping level, strain, structural defects, the dielectric environment, intrinsic band structure, and many body effects in low dimensional structures, may play roles in the detected signals.[34−38] A more systematic investigation of such complex phenomenon is ongoing. The findings also indicate the superior capability of s-SNOM for estimating the quality of two-dimensional plasmonic materials, which can be used to optimize the CVD growth parameters.[39,40]

To sum up, controlled synthesis of large-area *h*-G-*h*-BN in-plane heterostructure arrays has been realized by a continuous one-pot APCVD method. Within the heterostructure, the inner hexagonal graphene crystal is well connected with the outer *h*-BN ribbons, showing a uniform continuity across the whole surface. Intensive measurements suggest that the BN growth is highly templated by the edges of the first-grown graphene hexagons. By controlling the growth time of BN, a centimeter-scale uniform monolayer hybrid film composed of ordered G and *h*-BN is prepared. Furthermore, our study shows the superior capability of s-SNOM for estimating the quality of two-dimensional plasmonic materials. Our approach may have significant impact on scalable syntheses of large-area 2D heterostructure arrays and paves the way for the development of future flexible two-dimensional electronic and photonic devices.

■ ASSOCIATED CONTENT

Supporting Information

The Supporting Information is available free of charge at https://pubs.acs.org/doi/10.1021/acsmaterialslett.0c00517.

Procedures and additional data (PDF)

■ AUTHOR INFORMATION

Corresponding Authors

Dechao Geng − *Pillar of Engineering Product Development, Singapore University of Technology and Design, Singapore 487372, Singapore; Tianjin Key Laboratory of Molecular Optoelectronic Sciences, Department of Chemistry, School of Science, Tianjin University, Tianjin 300072, China*; Email: gengdechao_1987@tju.edu.cn

Lin Li − *Institute of Molecular Plus, Tianjin University, Tianjin 300072, China*; Email: linli2020@tju.edu.cn

Hui Ying Yang − *Pillar of Engineering Product Development, Singapore University of Technology and Design, Singapore 487372, Singapore*; orcid.org/0000-0002-2244-8231; Email: yanghuiying@sutd.edu.sg

Authors

Ibrahim Abdelwahab − *Department of Chemistry, National University of Singapore, Singapore 117543, Singapore*; orcid.org/0000-0002-0107-5827

Xiaofei Xiao − *The Blackett Laboratory, Department of Physics, Imperial College London, London SW7 2AZ, United Kingdom*

Adrian Cernescu − *Neaspec GmbH, Haar 85540, Munich, Germany*

Wei Fu − *Department of Chemistry, National University of Singapore, Singapore 117543, Singapore*

Vincenzo Giannini − *The Blackett Laboratory, Department of Physics, Imperial College London, London SW7 2AZ, United Kingdom*

Stefan A. Maier − *The Blackett Laboratory, Department of Physics, Imperial College London, London SW7 2AZ, United Kingdom; Nanoinstitute Munich, Faculty of Physics, Ludwig-*

https://dx.doi.org/10.1021/acsmaterialslett.0c00517
ACS Materials Lett. 2021, 3, 217−223

Maximilians-Universität München, 80539 München, Germany

Wenping Hu − *Tianjin Key Laboratory of Molecular Optoelectronic Sciences, Department of Chemistry, School of Science, Tianjin University, Tianjin 300072, China;* orcid.org/0000-0001-5686-2740

Kian Ping Loh − *Department of Chemistry, National University of Singapore, Singapore 117543, Singapore; Joint School of National University of Singapore and Tianjin University, International Campus of Tianjin University, Binhai New City, Fuzhou 350207, China;* orcid.org/0000-0002-1491-743X

Complete contact information is available at: https://pubs.acs.org/10.1021/acsmaterialslett.0c00517

Author Contributions

D.C.G. and I.A. contributed equally to this work.

Notes

The authors declare no competing financial interest.

■ ACKNOWLEDGMENTS

This research is supported by Singapore MOE academic research grant Tier 2 (MOE2018-T2-2-178) and National Natural Science Foundation of China (52002267). K.P.L. would like to acknowledge National Research Foundation (Singapore) Grant "NRF-CRP22-2019-0006: Geometric Interface Optics: A Synthetic Platform for High-capacity & Low-dimensional Metaphotonics".

■ REFERENCES

(1) Yuan, G. W.; Lin, D. J.; Wang, Y.; Huang, X. L.; Chen, W.; Xie, X. D.; Zong, J. Y.; Yuan, Q. Q.; Zheng, H.; Wang, D.; Xu, J.; Li, S. C.; Zhang, Y.; Sun, J.; Xi, X. X.; Gao, L. B. *Nature* **2020**, *577*, 204−208.
(2) Li, X. S.; Cai, W. W.; An, J.; Kim, S.; Nah, J.; Yang, D. X.; Piner, R.; Velamakanni, A.; Jung, I.; Tutuc, E.; Banerjee, S. K.; Colombo, L.; Ruoff, R. S. *Science* **2009**, *324*, 1312.
(3) Chen, J. H.; Jang, C.; Xiao, S.; Ishigami, M.; Fuhrer, M. S. *Nat. Nanotechnol.* **2008**, *3*, 206−209.
(4) Shi, Z. Y.; Wang, X. J.; Li, Q. T.; Yang, P.; Lu, G. Y.; Jiang, R.; Wang, H.; Zhang, C.; Cong, C. X.; Liu, Z.; Wu, T. R.; Wang, H. M.; Yu, Q. K.; Xie, X. M. *Nat. Commun.* **2020**, *11*, e849.
(5) Wang, L.; Xu, X. Z.; Zhang, L. N.; Qiao, R. X.; Wu, M. H.; Wang, Z. C.; Zhang, S.; Liang, J.; Zhang, Z. H.; Zhang, Z. B.; Chen, W.; Xie, X. D.; Zong, J. Y.; Shan, Y. W.; Guo, Y.; Willinger, M.; Wu, H.; Li, Q. Y.; Wang, W. L.; Gao, P.; Wu, S. W.; Zhang, Y.; Jiang, Y.; Yu, D. P.; Wang, E. G.; Bai, X. D.; Wang, Z. J.; Ding, F.; Liu, K. H. *Nature* **2019**, *570*, 91−95.
(6) Chen, T.-A.; Chuu, C.-P.; Tseng, C.-C.; Wen, C.-K.; Wong, H.-S. P.; Pan, S.; Li, R.; Chao, T.-A.; Chueh, W.-C.; Zhang, Y.; Fu, Q.; Yakobson, B. I.; Chang, W.-H.; Li, L.-J. *Nature* **2020**, *579*, 219−223.
(7) Tang, S. J.; Wang, H. M.; Wang, H.S.; Sun, Q. J.; Zhang, X. Y.; Cong, C. X.; Xie, H.; Liu, X. Y.; Zhou, X. H.; Huang, F. Q.; Chen, X. S.; Yu, T.; Ding, F.; Xie, X. M.; Jiang, M. H. *Nat. Commun.* **2015**, *6*, e6499.
(8) Chen, L. X.; He, L.; Wang, H. S.; Wang, H. M.; Tang, S. J.; Cong, C. X.; Xie, H.; Li, L.; Xia, H.; Li, T. X.; Wu, T. R.; Zhang, D. L.; Deng, L. W.; Yu, T.; Xie, X. M.; Jiang, M. H. *Nat. Commun.* **2017**, *8*, e14703.
(9) Ci, L.; Song, L.; Jin, C.; Jariwala, D.; Wu, D.; Li, Y.; Srivastava, A.; Wang, Z. F.; Storr, K.; Balicas, L.; Liu, F.; Ajayan, P. M. *Nat. Mater.* **2010**, *9*, 430.
(10) Liu, L.; Park, J.; Siegel, D. A.; McCarty, K. F.; Clark, K. W.; Deng, W.; Basile, L.; Idrobo, J. C.; Li, A.-P.; Gu, G. *Science* **2014**, *343*, 163.
(11) Wang, H. S.; Chen, L.; Elibol, K.; He, L.; Wang, H. M.; Chen, C.; Jiang, C. X.; Li, C.; Wu, T. R.; Cong, C. X.; Pennycook, T. J.; Argentero, G.; Zhang, D. L.; Watanabe, K.; Taniguchi, T.; Wei, W. Y.; Yuan, Q. H.; Meyer, J. C.; Xie, X. M. *Nat. Mater.* **2020**, DOI: 10.1038/s41563-020-00806-2.
(12) Gao, T.; Song, X. J.; Du, H. W.; Nie, Y. F.; Chen, Y. B.; Ji, Q. Q.; Sun, J. Y.; Yang, Y. L.; Zhang, Y. F.; Liu, Z. F. *Nat. Commun.* **2015**, *6*, 6835.
(13) Sediri, H.; Pierucci, D.; Hajlaoui, M.; Henck, H.; Patriarche, G.; Dappe, Y. J.; Yuan, S.; Toury, B.; Belkhou, R.; Silly, M. G.; Sirotti, F.; Boutchich, M.; Ouerghi, A. *Sci. Rep.* **2015**, *5*, e16465.
(14) Ramasubramaniam, A.; Naveh, D. *Phys. Rev. B: Condens. Matter Mater. Phys.* **2011**, *84*, 075405.
(15) Pruneda, J. M. *Phys. Rev. B: Condens. Matter Mater. Phys.* **2010**, *81*, 161409.
(16) Liu, Z.; Ma, L. L.; Shi, G.; Zhou, W.; Gong, Y. J.; Lei, S. D.; Yang, X. B.; Zhang, J. N.; Yu, J. J.; Hackenberg, K. P.; Babakhani, A.; Idrobo, J. C.; Vajtai, R.; Lou, J.; Ajayan, P. M. *Nat. Nanotechnol.* **2013**, *8*, 119.
(17) Levendorf, M. P.; Kim, C. J.; Brown, L.; Huang, P. Y.; Havener, R. W.; Muller, D. A.; Park, J. *Nature* **2012**, *488*, 627.
(18) Geng, D. C.; Wu, B.; Guo, Y. L.; Huang, L. P.; Xue, Y. Z.; Chen, J. Y.; Yu, G.; Jiang, L.; Hu, W. P.; Liu, Y. Q. *Proc. Natl. Acad. Sci. U. S. A.* **2012**, *109*, 7992.
(19) Lu, G. Y.; Wu, T. R.; Yang, P.; Yang, Y. C.; Jin, Z. H.; Chen, W. B.; Jia, S.; Wang, H. M.; Zhang, G. H.; Sun, J. L.; Ajayan, P. M.; Lou, J.; Xie, X. M.; Jiang, M. H. *Adv. Sci.* **2017**, *4*, e1700076.
(20) Han, G. H.; Rodríguez-Manzo, J. A.; Lee, C. W.; Kybert, N. J.; Lerner, M. B.; Qi, Z. Q.; Dattoli, E. N.; Rappe, A. M.; Drndic, M.; Johnson, A. T. C. *ACS Nano* **2013**, *7*, 10129.
(21) Geng, D. C.; Luo, B. R.; Xu, J.; Guo, Y. L.; Wu, B.; Hu, W. P.; Liu, Y. Q.; Yu, G. *Adv. Funct. Mater.* **2014**, *24*, 1664.
(22) Tan, L. F.; Han, J. L.; Mendes, R. G.; Rümmeli, M. H.; Liu, J. X.; Wu, Q.; Leng, X. Y.; Zhang, T.; Zeng, M. Q.; Fu, L. *Adv. Electron. Mater.* **2015**, *1*, e1500223.
(23) Wang, L. F.; Wu, B.; Chen, J. S.; Liu, H. T.; Hu, P. A.; Liu, Y. Q. *Adv. Mater.* **2014**, *26*, 1559.
(24) Song, X. J.; Gao, J. F.; Nie, Y. F.; Gao, T.; Sun, J. Y.; Ma, D. L.; Li, Q. C.; Chen, Y. B.; Jin, C. H.; Bachmatiuk, A.; Rümmeli, M. H.; Ding, F.; Zhang, Y. F.; Liu, Z. F. *Nano Res.* **2015**, *8*, 3164.
(25) Tay, R. Y.; Park, H. J.; Ryu, G. H.; Tan, D.; Tsang, S. H.; Li, H.; Liu, W.; Teo, E. H.; Lee, Z.; Lifshitz, Y.; Ruoff, R. S. *Nanoscale* **2016**, *8*, 2434.
(26) McCreary, K. M.; Currie, M.; Hanbicki, A. T.; Chuang, H. J.; Jonker, B. T. *ACS Nano* **2017**, *11*, 7988−7994.
(27) Cong, C. X.; Shang, J. Z.; Wu, X.; Cao, B. C.; Peimyoo, N.; Qiu, C.; Sun, L. T.; Yu, T. *Adv. Opt. Mater.* **2014**, *2*, 131−136.
(28) Lu, X. W.; Khatib, O.; Du, X. T.; Duan, J. H.; Wei, W.; Liu, X. L.; Bechtel, H. A.; D'Apuzzo, F.; Yan, M. T.; Buyanin, A.; Fu, Q.; Chen, J. N.; Salmeron, M.; Zeng, J.; Raschke, M. B.; Jiang, P.; Bao, X. H. *Adv. Electron. Mater.* **2018**, *4*, 1700377.
(29) Lin, L.; Zhang, J.; Su, H.; Li, J.; Sun, L.; Wang, Z.; Xu, F.; Liu, C.; Lopatin, S.; Zhu, Y.; Jia, K.; Chen, S.; Rui, D.; Sun, J.; Xue, R.; Gao, P.; Kang, N.; Han, Y.; Xu, H. Q.; Cao, Y.; Novoselov, K. S.; Tian, Z.; Ren, B.; Peng, H. L.; Liu, Z. F. *Nat. Commun.* **2019**, *10*, e1912.
(30) Ci, L.; Song, L.; Jin, C. H.; Jariwala, D.; Wu, D.; Li, Y.; Srivastava, A.; Wang, Z. F.; Storr, K.; Balicas, L.; Liu, F.; Ajayan, P. M. *Nat. Mater.* **2010**, *9*, 430−435.
(31) Bepete, G.; Voiry, D.; Chhowalla, M.; Chiguvare, Z.; Coville, N. J. *Nanoscale* **2013**, *5*, 6552−6557.
(32) Lee, J.; Novoselov, K. S.; Shin, H. S. *ACS Nano* **2011**, *5*, 608−612.
(33) Ansari, N.; Nazari, F.; Illas, F. *Phys. Chem. Chem. Phys.* **2014**, *16*, 21473−21485.
(34) Esrafili, M. D. *Phys. Lett. A* **2019**, *383*, 1607−1614.
(35) Guo, X. D.; Hu, H.; Hu, D.; Liao, B.; Chen, K.; Liu, L.; Zhu, X.; Yang, X.; Dai, Q. *Nanoscale* **2019**, *11*, 2703−2709.

(36) Palik, E. D. *Handbook of Optical Constants of Solids*; Academic Press, Boston, 1985.
(37) Li, P.; Dolado, I.; Alfaro-Mozaz, F. J.; Nikitin, A. Y.; Casanova, F.; Hueso, L. E.; Vélez, S.; Hillenbrand, R. *Nano Lett.* **2017**, *17*, 228−235.
(38) Nikitin, A. Y.; Alonso-González, P.; Vélez, S.; Mastel, S.; Centeno, A.; Pesquera, A.; Zurutuza, A.; Casanova, F.; Hueso, L. E.; Koppens, F. H. L.; Hillenbrand, R. *Nat. Photonics* **2016**, *10*, 239−243.
(39) Chen, L. X.; Wang, H. M.; Tang, S. J.; He, L.; Wang, H. S.; Wang, X. J.; Xie, H.; Wu, T. R.; Xia, H.; Li, T. X.; Xie, X. M. *Nanoscale* **2017**, *9*, 11475.
(40) Ma, T.; Ren, W. C.; Zhang, X. Y.; Liu, Z. B.; Gao, Y.; Yin, L. C.; Ma, X. L.; Ding, F.; Cheng, H. M. *Proc. Natl. Acad. Sci. U. S. A.* **2013**, *110*, 20386.

https://dx.doi.org/10.1021/acsmaterialslett.0c00517
ACS Materials Lett. 2021, 3, 217−223